Key Points:
- An objective detection technique for tracking tropical cyclone extratropical transition in gridded climate data is described
- Objectively calculated extratropical transition climatology in high-resolution reanalyses closely match observational studies
- Tropical cyclones in CAM take too long to undergo extratropical transition highlighting model biases requiring further investigation

Objective tropical cyclone extratropical transition detection in high-resolution reanalysis and climate model data

Colin M. Zarzycki[1] (iD), Diana R. Thatcher[2], and Christiane Jablonowski[2]

[1]National Center for Atmospheric Research, Boulder, Colorado, USA, [2]Climate and Space Sciences and Engineering, University of Michigan, Ann Arbor, Michigan, USA

Abstract This paper describes an objective technique for detecting the extratropical transition (ET) of tropical cyclones (TCs) in high-resolution gridded climate data. The algorithm is based on previous observational studies using phase spaces to define the symmetry and vertical thermal structure of cyclones. Storm tracking is automated, allowing for direct analysis of climate data. Tracker performance in the North Atlantic is assessed using 23 years of data from the variable-resolution Community Atmosphere Model (CAM) at two different resolutions ($\Delta X \sim$ 55 km and 28 km), the Climate Forecast System Reanalysis (CFSR, $\Delta X \sim$ 38 km), and the ERA-Interim Reanalysis (ERA-I, $\Delta X \sim$ 80 km). The mean spatiotemporal climatologies and seasonal cycles of objectively detected ET in the observationally constrained CFSR and ERA-I are well matched to previous observational studies, demonstrating the capability of the scheme to adequately find events. High-resolution CAM reproduces TC and ET statistics that are in general agreement with reanalyses. One notable model bias, however, is significantly longer time between ET onset and ET completion in CAM, particularly for TCs that lose symmetry prior to developing a cold-core structure and becoming extratropical cyclones, demonstrating the capability of this method to expose model biases in simulated cyclones beyond the tropical phase.

1. Introduction

The transition of tropical cyclones (TCs) into extratropical cyclones (ETCs) is commonly observed at the end of TC lifetimes. Extratropical transition (ET) occurs as a mature TC moves over cooler water and into areas of stronger wind shear at higher latitudes. During this transition, the cyclone loses its symmetric, warm-core structure and distinct eyewall. The resulting ETC is a cold-core system possessing asymmetric, frontal structure. TCs may rapidly develop into fast-moving ETCs and threaten coastal regions with damaging precipitation, waves, and winds that are difficult to forecast. These storms can greatly impact midlatitude weather, particularly along the eastern side of ocean basins where TCs occur [*Jones et al.*, 2003; *Anwender et al.*, 2008].

Generally, ET occurs as a TC interacts with a midlatitude baroclinic system [*DiMego and Bosart*, 1982; *Sinclair*, 1993; *Harr and Elsberry*, 2000; *Harr et al.*, 2000]. Substantial variability exists in the complex interactions of TCs and large-scale systems [*Foley and Hanstrum*, 1994; *Ritchie and Elsberry*, 2007]. *Klein et al.* [2000] provide a conceptual model of ET, including TC interaction with a preexisting baroclinic system, transformation of the TC into a baroclinic low, and reintensification to form an ETC. This conceptual model is consistent with mesoscale model results by *Ritchie and Elsberry* [2001]. Reintensification may occur after the transition is completed depending on the surrounding large-scale atmospheric structures, such as the presence of upper-level troughs [*Ritchie and Elsberry*, 2003; *Hart et al.*, 2006].

ET is generally analyzed using reanalysis products based on observations [e.g., *Klein et al.*, 2000; *Hart and Evans*, 2001; *Sinclair*, 2002; *Studholme et al.*, 2015]. ET in global climate models has been largely ignored, in large part due to the high spatial resolution needed to adequately resolve TCs and the associated computational expense. Typically, global general circulation model (GCM) grid spacings of approximately 100 km are sufficient to simulate weak TCs, but the intense core, including convection in the eyewall, is unresolved [e.g., *Krishnamurti et al.*, 1989; *Walsh et al.*, 2015]. Recent work has shown that horizontal grid spacing must be at least 50 km to produce quasi-realistic TC climatology [*Bengtsson et al.*, 2007; *Zhao et al.*, 2009], although results that better match observations require even finer resolutions [*Strachan et al.*, 2013; *Wehner*

et al., 2014; *Zarzycki and Jablonowski*, 2014]. Given that climate models are growing more realistic in their representation of TCs, exploring ET associated with these storms is important to better understand model behavior and biases, as well as produce tangible science regarding climate impacts of partially or fully transitioned TCs.

This paper presents the description and implementation of an objective algorithm for detecting and tracking TCs and ET in high-resolution gridded climate data. This differs from traditional manual tracking methods in that a point observational data set is not required to first locate TCs in gridded data. This technique is used to quantify TCs that undergo ET and track subsequent ETCs in four different data sets; the Climate Forecast System Reanalysis (CFSR), the European Centre for Medium-Range Weather Forecasts (ECMWF) Interim Reanalysis (ERA-I), and two multidecadal, TC-permitting climate simulations at different horizontal resolutions in the Community Atmosphere Model (CAM). Specific focus will be paid to the North Atlantic basin for both comparison with past work as well as to exploit the computational benefits associated with variable-resolution CAM. The resultant TC and ET climatologies are contrasted between the four gridded products and compared to previous observational studies. Particular emphasis is placed on detailing how the tracker performs relative to prior observational work and discussing its potential usefulness in detecting and understanding biases in climate data with respect to ET.

The structure of this paper is as follows. Section 2 describes the data products used and the GCM setup. The algorithmic technique for tracking TCs and identifying ET occurrences is described in section 3. The results, including climatology and cyclone phase space analysis, for the model simulations and reanalyses are presented in section 4. Section 5 provides discussion and conclusions.

2. Data Products and Model Configuration

2.1. Observational Data and Reanalysis

Generalized parameters in an objective tracking algorithm require gridded data sets that are spatiotemporally continuous. Given this, observationally driven reanalyses are the most logical choice for assessing the historical record. Therefore, we utilize two such products in this analysis. First, is the Climate Forecast System Reanalysis (CFSR) [*Saha et al.*, 2010] product from National Centers for Environmental Prediction (NCEP). The resolution of the CFSR model is T382 (∼38 km), although the postprocessed data used for analysis are output on a 0.5° × 0.5° latitude-longitude grid over the 1980–2002 period. As described by *Schenkel and Hart* [2012], CFSR uses a unique system of TC vortex relocation in which a vortex is moved to the observed location based on the National Hurricane Center (NHC) Best-Track data set [*Jarvinen et al.*, 1984; *McAdie et al.*, 2009; *Landsea and Franklin*, 2013] or a vortex not initially present in CFSR is synthetically added. This improves the representation of TC intensity in the reanalysis product because the TC is placed in the correct large-scale environment. To compare to a reanalysis without TC-specific treatment during data assimilation, we also utilize the ECMWF Interim Reanalysis (ERA-I) [*Dee et al.*, 2011]. ERA-I is integrated at T255 (∼60 km) spectral resolution, with postprocessed output on a 0.7° × 0.7° latitude-longitude grid over the same time period as CFSR. For a more thorough description and an examination of the representation of TC position and intensity in CFSR and ERA-I, see *Schenkel and Hart* [2012].

The most obvious point observational data set to use for validation of algorithmic detection is the International Best Track Archive for Climate Stewardship (IBTrACS) TC best track database [*Knapp et al.*, 2010]. IBTrACS data in the North Atlantic (NATL) are compiled from quality-controlled records of TC data from the NHC. However, we note there are some drawbacks associated with using these data to also quantify ET. ET in IBTrACS is determined subjectively by various forecasters based on real-time observational data (e.g., satellite and surface observations) as opposed to being defined by a fixed, objective measure. In addition, IBTrACS phase transition occurs at an instantaneous point in space and time and provides no information about the path to (and duration of) ET. Finally, TC phases in IBTrACS can sometimes be inconsistent. For example, Hurricane Nadine (2012) is recorded as never having undergone ET, although the NHC's final storm report [*Brown*, 2013] indicates that the storm made a transition before dissipation. While a manual tracking method (similar to that in *Schenkel and Hart* [2012] for TCs or *Evans and Hart* [2003] for ET) could be applied, it would make evaluation of the detection algorithm presented here inconsistent with unconstrained model data (since there is no corresponding "point observation" data set for climate simulations). Therefore, we use IBTrACS as a supplement to CFSR and ERA-I, with the latter two being considered

"observational proxies" consistent with the spatially and temporally continuous format of climate model data to be analyzed.

2.2. Climate Model

The spectral element version of the Community Atmosphere Model (CAM-SE) is jointly developed by the National Center for Atmospheric Research and various Department of Energy laboratories. It utilizes a cubed-sphere grid with a continuous Galerkin spectral element method [*Taylor et al.*, 1997]. Energy, mass, and 2-D potential vorticity are locally conserved [*Taylor and Fournier*, 2010] and each element has third degree polynomial basis functions that provide fourth-order accuracy [*Dennis et al.*, 2012]. Because CAM-SE is designed for use with unstructured grids, arbitrary meshes are permitted so long as all elements tiling the sphere are quadrilateral and conforming [*Dennis et al.*, 2012]. This offers variable-resolution capabilities that allow for static regional refinement, greatly reducing computational cost for high-resolution simulations over a particular area of interest [*Zarzycki et al.*, 2014a, 2014b, 2015].

The model setup used here is similar to *Zarzycki and Jablonowski* [2014], who previously studied TC climatology in variable-resolution CAM. Two variable-resolution grids are used. Both configurations have a global base resolution of 1° (∼111 km) with one transitioning to a high-resolution region at 0.5° (∼55 km) over the NATL and a second that increases this refinement to 0.25° (∼28 km) over the same region. These grids will be referred to as CAM-55 and CAM-28, respectively, for the remainder of this manuscript and are shown in Figure 1. 30 vertical model levels are used with a model top of approximately 2 hPa. Unlike in the horizontal, the vertical resolution is globally constant.

The dynamics time step is 150 s (37.5 s) and the physics time step is 900 s (900 s) for the CAM-55 (CAM-28) simulation. Explicit fourth-order hyperdiffusion is applied to all elements, although the diffusion coefficient, K_4, depends on the size of the grid cell. The largest grid cells (1°) use $K_4 = 1 \times 10^{15}$ m^4 s^{-1}, the smallest grid cells (0.25°) use $K_4 = 1 \times 10^{13}$ m^4 s^{-1}. The grid cells between these resolutions are scaled based on the length of the longest axis of the grid cell [*Zarzycki et al.*, 2014b]. The simulation makes use of the CAM version 5 (CAM5) subgrid physical parameterizations [*Neale et al.*, 2010].

CAM is coupled to Community Earth System Model (CESM) ocean/ice and land components and the simulations follow Atmospheric Model Intercomparison Project (AMIP) protocols [*Gates*, 1992; *Gleckler*, 2004]. Prescribed sea surface temperatures (SSTs) are derived from the Hadley Centre Sea Ice and Sea Surface Temperatures (HadISST) data set [*Hurrell et al.*, 2008]. Atmospheric chemistry is also prescribed to reproduce observed greenhouse gas and aerosol concentrations over the study period. The Community Land Model (CLM) version 4.0 is not prescribed and is run on the same grid as the atmosphere in satellite phenology
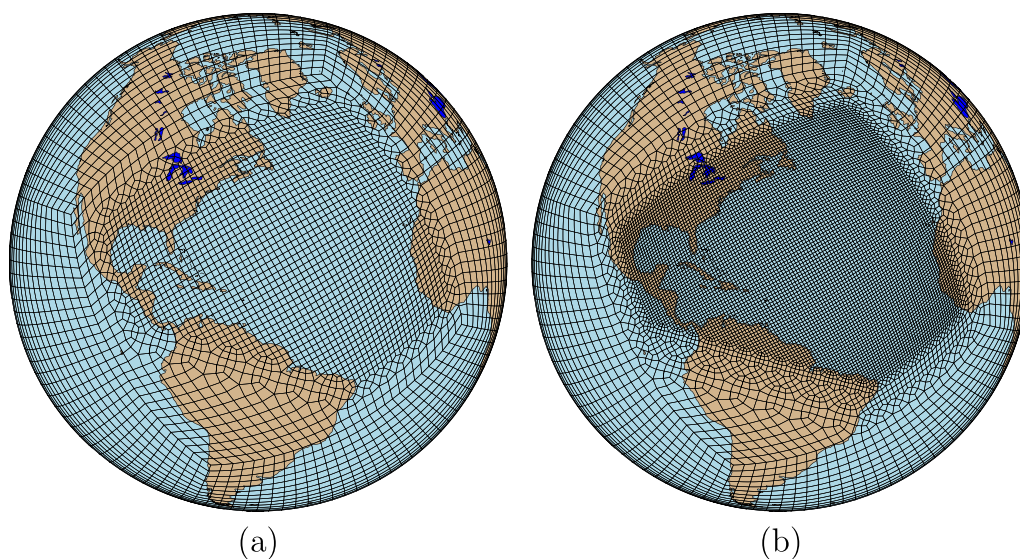

(a)   (b)

Figure 1. The two CAM-SE grids used for this study are (a) a variable resolution mesh that ranges from 1° → 0.5° and (b) a variable resolution mesh that ranges from 1° → 0.25°. Note that each element shown in the above plots contains additional 3 × 3 collocation cells.

(SP) mode [*Oleson et al.*, 2010]. Simulations were run from September 1979 until January 2003 with the first 4 months discarded for spin-up. It should be emphasized that since CAM is free running (i.e., no internal nudging and vortex seeding), simulations are not expected to reproduce specific TC trajectories as one would expect in CFSR and ERA-I. Focus is instead centered on assessing the mean climatology of both simulations and comparing to analogous statistics from CFSR and ERA-I.

Output data from both CAM simulations and ERA-I are conservatively remapped to the same $0.5° \times 0.5°$ latitude-longitude grid as CFSR by applying the method outlined in *Ullrich and Taylor* [2015] and *Ullrich et al.* [2016]. This ensures that there is no resolution bias due to the native grid output of CAM-55, CAM-28, and CFSR. Cursory analysis (not shown) indicates that this regridding has minimal impact on the general TC climatology in the 0.25° CAM-28 when compared to analyzing native grid output. Somewhat larger differences in climatology (in the two CAM simulations and CFSR) were noted if all data were degraded to match ERA-I ($0.7° \times 0.7°$), therefore the choice was made not to coarsen beyond the CFSR postprocessed grid.

3. Tracking Method

3.1. Tropical Cyclone Tracking

Individual TCs in 6 hourly CAM, CFSR, and ERA-I data are tracked using TempestExtremes [*Ullrich and Zarzycki*, 2016]. A brief overview of the technique used is presented here, although a more comprehensive discussion of the general procedure for detecting TCs can be found in *Zarzycki and Jablonowski* [2014] (note that the parameter values are slightly different in this study). First, candidate storms are detected at 6 h time intervals by ensuring that a sea level pressure (SLP) minimum is surrounded by a closed contour of SLP 2 hPa greater than the minimum within 5°. This is defined as the TC center. A geopotential thickness maximum between the 300 and 500 hPa levels is used as a thermal criterion to eliminate storms lacking warm cores. This maximum must be spatially aligned with the SLP minimum (no more than 1° offset in the horizontal) and be enclosed by a closed ring of thickness 5 m less than the maximum. This closed contour must fully lie within 5° of the thickness maximum. Candidate cyclones are then stitched together in time, with storms needing to be equatorward of 40° latitude for at least 60 h (not necessarily consecutive). Storm translational speed is restricted to 25 m s^{-1} and separate trajectories which terminate and begin within 12 h and 10° of one another are merged to eliminate double counting of broken tracks.

3.2. Extratropical Cyclone Tracking

Once the TC trajectory is terminated in the above method, a separate ETC tracking algorithm is used to determine the continued trajectory of the storm. Starting with the final point of the TC trajectory, the storm is tracked by following the local minimum of SLP. Based on the ETC tracking method described in *Hart* [2003], the translational speed of the storm is limited to 40 m s^{-1} and changes in movement direction are limited based on the storm's speed. The first requirement reduces the search area for the next location of the storm to a reasonable size. The second requirement prevents the storm from making unrealistic sharp turns when fast moving. Both of these requirements reduce the number of potential local minima and prevent the tracking algorithm from jumping from the correct low-pressure system to another nearby pressure minimum. In the case that multiple local pressure minima fulfill these requirements, as often occurs when two midlatitude low-pressure systems are merging, the lowest pressure is tracked. Trajectories where the cyclone may split always follow the lowest SLP minimum (i.e., no new trajectories are generated once a storm leaves the tropical phase).

The ETC is tracked until the storm dissipates or exits the NATL domain. This domain is defined to be from 10°N to 75°N and 110°W to 20°E. Any storms that exit the domain below 10°N are considered to have left the domain as tropical storms without transitioning. The ETC is also considered dissipated if the minimum SLP rises above 1020 hPa.

3.3. Definition of Extratropical Transition

Quantifying ET in high-resolution gridded data requires an objective method for determining the onset and completion of ET. In observational records, such as IBTrACS, the transition of a TC is subjectively defined using a variety of factors. For example, satellite imagery will show a TC losing its compact, symmetrical structure as it gradually expands and the distribution of clouds and precipitation becomes asymmetrical. Climatologies of ET using observations are available for the North Atlantic [*Hart and Evans*, 2001], western

North Pacific [*Klein et al.*, 2000], southwest Pacific [*Sinclair*, 2002], and the west coast of Australia [*Foley and Hanstrum*, 1994].

Here we require objective criteria that can be used to automatically track the transition from TC to ETC in both gridded reanalysis and model data. To do so, we use the parameter framework in *Hart* [2003]. The storm region includes all data points within a 500 km radius of the cyclone center (minimum SLP). The 500 km radius is defined on the sphere using the great-circle distance between all nearby grid points and the center of the cyclone. The direction of the storm's motion is calculated by applying a backward difference with the current storm location and prior location (6 h before).

The symmetric (nonfrontal) or asymmetric (frontal) nature of the storm is determined by the 900–600 hPa thickness asymmetry, B:

$$B = h\left(\overline{Z_{600\,hPa} - Z_{900\,hPa}}\big|_R - \overline{Z_{600\,hPa} - Z_{900\,hPa}}\big|_L\right) \tag{1}$$

where Z is geopotential height at the 600 and 900 hPa pressure levels. CAM uses a hybrid sigma-pressure vertical coordinate, therefore, the data are interpolated to constant pressure levels. R and L indicate the semicircles on the right and left sides of the storm relative to storm motion. The overbar indicates that the average is taken over the entire semicircle within a 500 km radius from the center of the storm. The integer h is $+1$ in the Northern Hemisphere and -1 in the Southern Hemisphere. Therefore, B measures the difference in the mean 900–600 hPa geopotential thickness between the right and left sides of the storm. In this study, symmetric storms, such as TCs, have B values below 15 and asymmetric storms, such as ETCs, have B values above 15. Note, that this choice of threshold is different than that from *Hart* [2003], who used a value of 10. Here 15 is chosen because using a value of 10 with higher-resolution data sets tended to cause brief, false alarm ET events at low latitudes. Using cluster analysis, *Studholme et al.* [2015] found a mean B value of 13 for ET in the North Atlantic, indicating that the choice of 15 is reasonable.

The cold-core or warm-core structure of the storm is determined using the vertical derivative of the height perturbation, $\Delta Z = Z_{max} - Z_{min}$, as defined by *Hart* [2003]. The height perturbation ΔZ is measured as the difference between the maximum and minimum geopotential height on a pressure level within 500 km of the storm's center. The "cyclone thermal wind" is defined in the lower troposphere as

$$-V_T^L = \frac{\partial(\Delta Z)}{\partial \ln p}\bigg|_{900\,hPa}^{600\,hPa} \tag{2}$$

and in the upper troposphere as

$$-V_T^U = \frac{\partial(\Delta Z)}{\partial \ln p}\bigg|_{600\,hPa}^{300\,hPa} \tag{3}$$

where a linear regression fit over seven pressure levels gives the vertical profile of ΔZ. The pressure levels range from 300 to 600 hPa and from 600 to 900 hPa in 50 hPa increments. Once again, the geopotential height in CAM is interpolated from the model's hybrid coordinates. In warm-core storms, such as TCs, the isobaric height gradient decreases with height and $-V_T$ is positive. In cold-core storms, such as ETCs, the isobaric height gradient increases with height and $-V_T$ is negative.

B, $-V_T^L$, and $-V_T^U$ constitute what is known as a cyclone phase space (CPS). See *Hart* [2003] for further description of the CPS parameters used here. This CPS method has been used to study observed ET in the North Atlantic [*Evans and Hart*, 2003], western North Pacific [*Kitabatake*, 2011; *Song et al.*, 2011], and eastern North Pacific [*Wood and Ritchie*, 2014].

This CPS quantitatively describes the state of a cyclone during the entirety of its life cycle, enabling objective definitions of TCs, ETCs, and the transition from tropical to extratropical [*Hart*, 2003]. TCs have $B < 15$ and $-V_T^L > 0$. ETCs have $B > 15$ and $-V_T^L < 0$. ET onset is defined when either B first becomes greater than 15 or when $-V_T^L$ becomes less than 0. ET completion occurs when the alternate criteria is subsequently satisfied. ET duration is defined as the time between these ET onset and ET completion. CAM, CFSR, and ERA-I data are analyzed every 6 h (00Z, 06Z, 12Z, and 18Z). A cyclone must satisfy each criterion for at least 12 consecutive hours before it is considered to have formally undergone ET. To minimize short-term outlier changes in cyclone structure, 6 h CPS trajectory values are smoothed using a 24 h running mean after
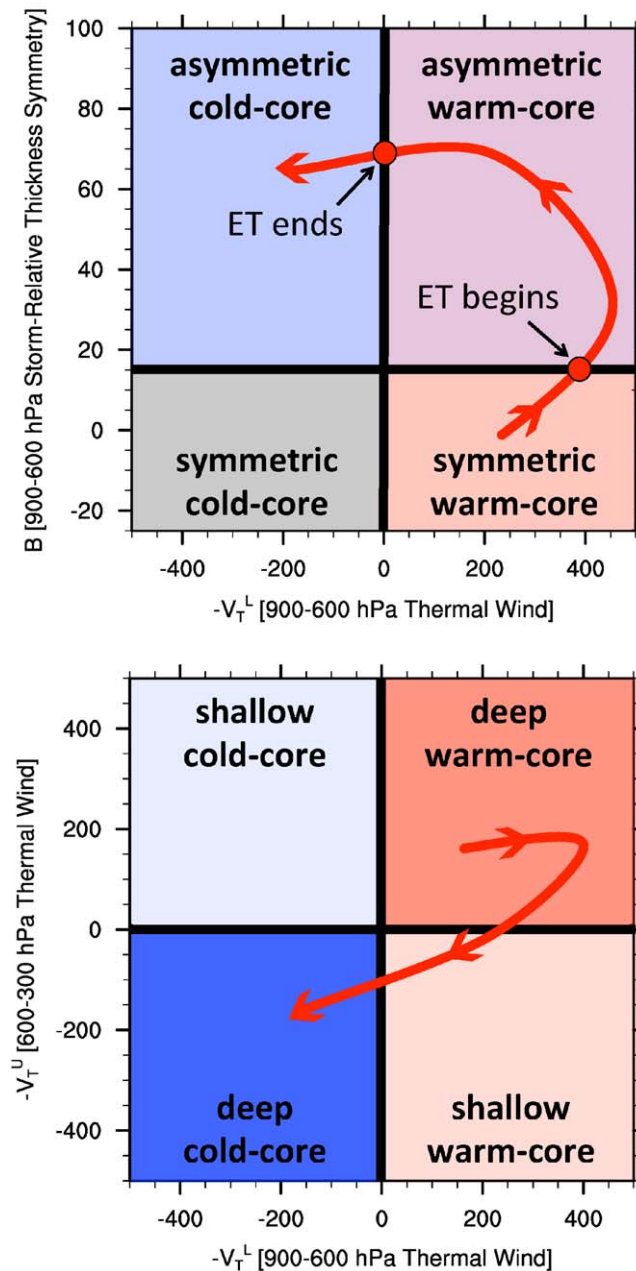
Figure 2. Overview of the cyclone phase space diagram. In this case, ET begins when $B > 15$ and ends when $-V_T^L < 0$.

cyclone tracking and the calculation of the above parameters but before determination of cyclone phase is completed.

A commonly used visual overview of CPS is shown in Figure 2. The top plot compares the B and $-V_T^L$ parameters that define the asymmetry and thermal structure, respectively. A typical TC begins in the bottom right quadrant (symmetric warm core). ET begins when a TC moves into either the top right (lose symmetry) or bottom left (lose warm core) quadrants. ET is complete as the storm moves into the top left quadrant, representing an asymmetric cold-core structure.

The bottom plot in Figure 2 compares the thermal structure in the lower and upper atmosphere. A typical TC will move into the upper right quadrant as it gains a deep warm-core structure, representing an intensifying hurricane, then gradually move to the bottom left quadrant as the thermal structure transitions to shallow warm core and then deep cold core.

Examples of the phase space diagram for two individual storms in CAM-28 and CFSR are shown in Figures 3 and 4. The left plots show the CPS over the lifetime of each cyclone and the right plot shows the trajectory of each storm. A colored marker indicating the minimum surface pressure of the cyclone is plotted every 12 h. Figure 3 shows a simulated hurricane in CAM-28. The top plot of the phase space diagram shows the TC transitioning from a symmetric warm core in the lower troposphere before developing asymmetric structure (ET onset is denoted by an "cross"). Following this, the TC eventually loses warm-core characteristics, completing its transi-

tion as a cold-core cyclone (ET completion is denoted by a hollow square). In the bottom plot, the TC develops a very deep warm core, with a strong warm-core structure in both the lower ($-V_L^T \approx 250$) and upper ($-V_U^T \approx 300$) troposphere. The deep warm-core structure weakens as the cyclone transitions, and the cyclone eventually exits the domain with a cold-core structure. This is common behavior of a strong hurricane undergoing ET in the North Atlantic [*Hart*, 2003].

Figure 4 shows a similar plot for a hurricane (Hurricane Floyd, 1999) in the CFSR data. Note that although Hurricane Floyd was actually a very strong TC, CFSR is not able to fully resolve the intensity of the storm, with the lowest minimum surface pressure being approximately 965 hPa in CFSR (921 hPa in IBTrACS). While
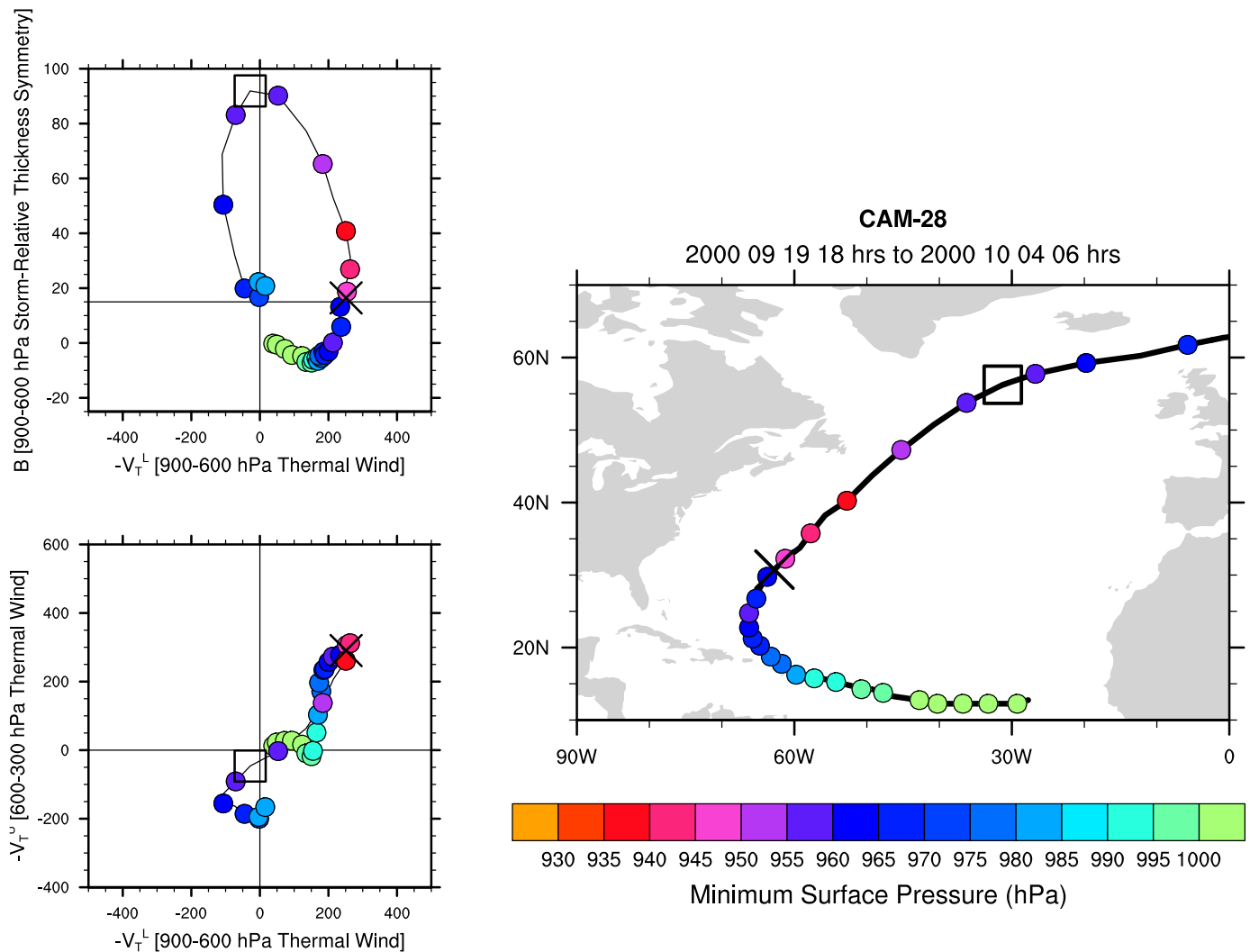
Figure 3. Example phase space diagram for a hurricane in CAM-SE. Data are plotted every 6 h with a colored marker every 12 h. Colors indicate the minimum sea level pressure (hPa) of the cyclone. The beginning of ET is marked with an cross and the end of ET is marked with a square.

the maximum value of $-V_L^T$ is about 200 and the maximum value of $-V_U^T$ is about 275, these values are not necessarily representative of all gridded products. For example, *Studholme et al.* [2015] found maximum values of $-V_L^T$ and $-V_U^T$ of about 300 and 400, respectively, in the European Center for Medium-range Weather Forecasting (ECMWF) operational analysis for storms of similar intensity to Floyd. Although these example cyclone phase diagrams only represent two individual storms, they give insight into how the tracker performs from a mechanistic standpoint.

4. Results

4.1. Climatology
4.1.1. Tropical Cyclones
While this work primarily focuses on corresponding ET associated with TCs, an understanding of the mean TC properties in the data sets is important to contextualize later discussion. The climatologies of NATL TCs in both CAM variable-resolution simulations, CFSR, ERA-I, and IBTrACS are compared for 1980–2002 with the annual mean number of tracked TCs shown in Figure 5. TCs are binned by Saffir-Simpson category [*Simpson*, 1974]. Tropical depressions and storms (TDs/TSs) are TCs with surface wind speeds ≤ 32 m s^{-1}. Hurricanes (in the NATL) are defined as any storm Category 1 or greater (>32 m s^{-1}). Intensity increases with
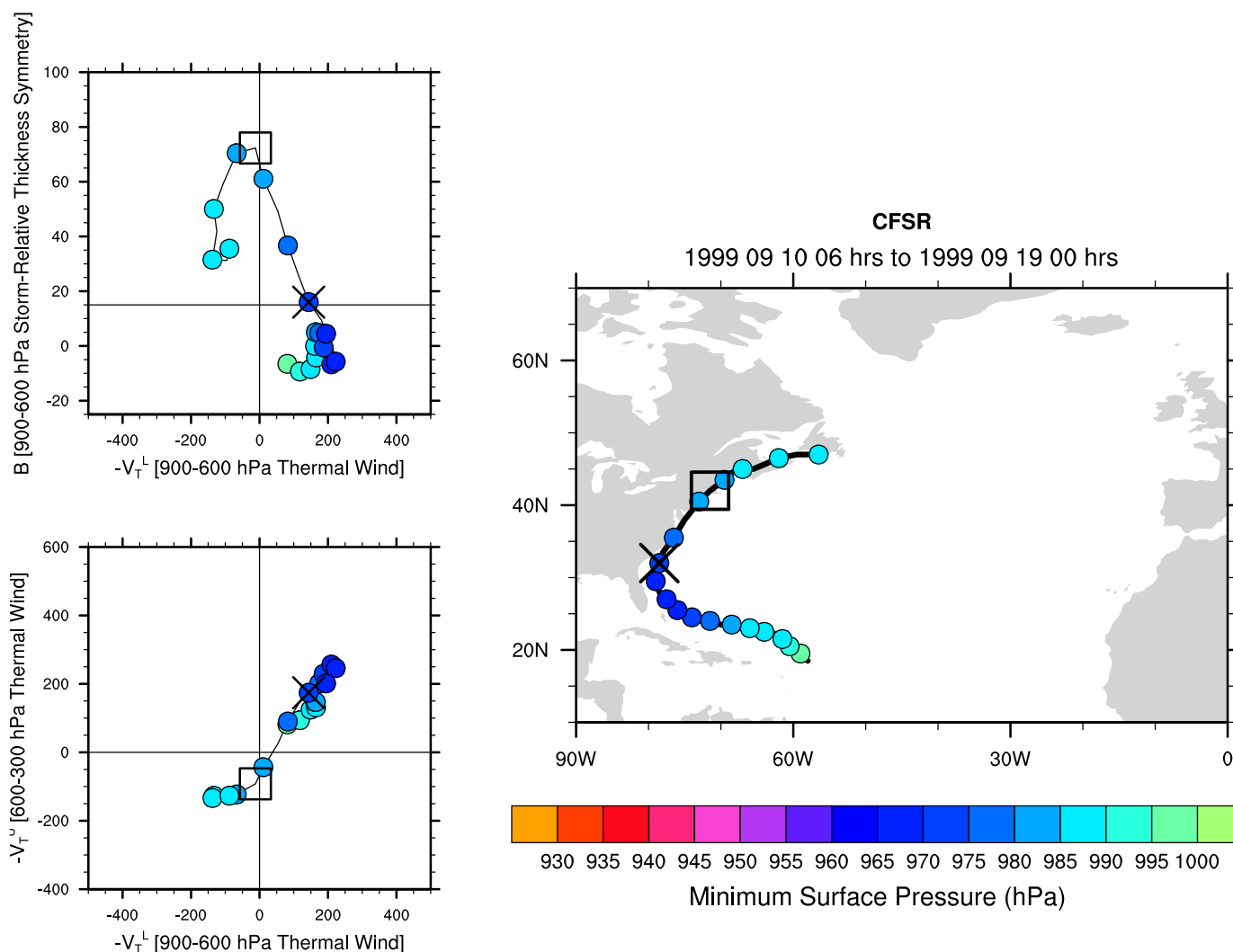
Figure 4. Same as Figure 3, except for a hurricane (Floyd, 1999) in CFSR.

increasing category—storms Cat. 3 and higher (≥ 50 m s^{-1}) are generally considered "major hurricanes." The cumulative sum of all categories is the total number of TCs per year.

It is readily apparent that increasing resolution from 55 to 28 km in the CAM simulations both increases the total number of simulated TCs (7.7 TCs per year versus 10.8 TCs per year) and shifts the distribution toward more intense TCs (e.g., CAM-28 produces 13% more TDs/TSs than CAM-55, but 500% more Cat. 3 hurricanes). Fewer total TCs are detected in ERA-I (3.8 TCs per year) due to the coarse grid spacing and lack of TC-specific treatment. CFSR produces a similar number of TCs (7.5 TCs per year) to CAM-55, but less than CAM-28. To an extent, this agrees with the fact that the nominal resolution of CFSR (38 km) is between that of the two CAM simulations and grid resolution has been shown to be correlated with TC intensity [*Walsh et al.*, 2007, 2015]. However, model configuration appears to also play a significant role in the intensity of TCs, with the CAM-55 simulations able to produce more Cat. 2 storms than CFSR, even at a coarser grid spacing.

CAM-55, CFSR, and ERA-I all produce less TCs than observations (IBTrACS, black, 10.7 TCs per year), with CAM-28 producing roughly the correct observed count. This is in agreement with CAM results from *Zarzycki and Jablonowski* [2014], as well as studies investigating algorithmically tracked TCs in CFSR and/or ERA-I [*Strachan et al.*, 2013; *Murakami*, 2014]. Even though reanalysis products are strongly nudged toward observations, issues such as the small size of TCs relative to model grid spacing and varying degrees of data coverage available for assimilation reduce the ability of the TC tracking algorithm to detect TCs, particularly
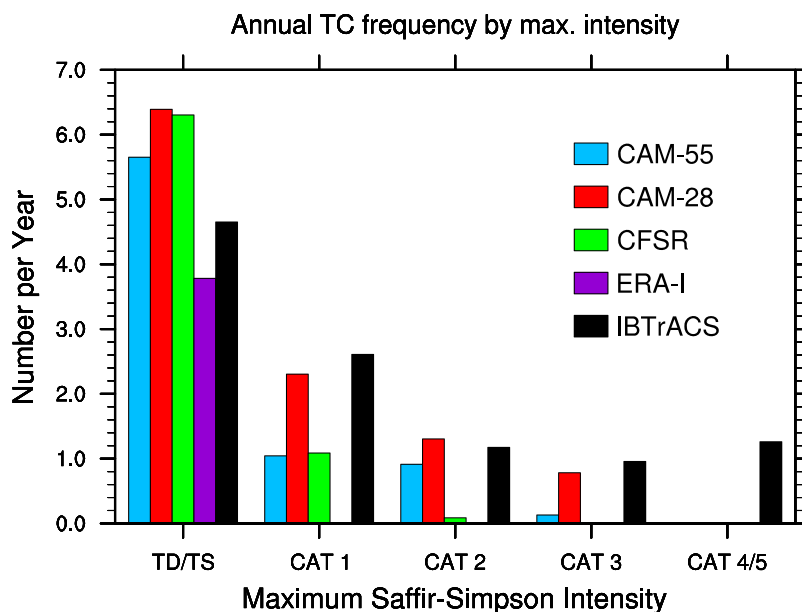
Figure 5. Mean annual number of objectively tracked NATL TCs over the 1980–2002 time period stratified by Saffir-Simpson category for CAM-55 (blue) and CAM-28 (red) simulations as well as CFSR (green) and ERA-I (purple) reanalysis data. The number of observed TCs in IBTrACS (black) are also shown for reference.

weak ones [*Schenkel and Hart*, 2012]. Using IBTrACS latitude-longitude pairs as truth over the 1980–2002 period, the tracking algorithm had a 65% (34%) hit rate for all observed NATL TCs, a 85% (55%) hit rate for all hurricanes, and a 17% (4%) false alarm rate when using CFSR (ERA-I). These numbers are similar to those in previous published studies [*Murakami*, 2014] and underscore the lack of resolved gradients in TC cores [*Schenkel and Hart*, 2012], likely implying that weaker storms are not adequately captured by either the climate model or reanalysis. Hit rates can be improved by relaxing the detection thresholds from section 3.1, however, cursory sensitivity analysis shows that when this is done false alarm rates (detection of TCs in reanalyses that are not recorded in IBTrACS) increase faster than the number of successful hits. Rigorous improvement in tuning thresholds is beyond the scope of this paper but is an area of ongoing research. For reasons mentioned above, explicit hit and false alarm rates cannot be calculated for free-running CAM simulations, but generalized assessments of CAM TC climatological skill can be found in *Bacmeister et al.* [2014], *Zarzycki and Jablonowski* [2014], and *Wehner et al.* [2014].

4.1.2. Extratropical Transitions

Table 1 shows the number of TCs (sum of all categories in Figure 5 over 23 years) and corresponding ETs for the two CAM simulations and two reanalyses. Of the 178 (248) total TCs in CAM-55 (CAM-28), 72 (121) were classified as undergoing ET. In comparison, CFSR (ERA-I) had 172 (87) TCs, of which 86 (48) become ETCs before either dissipating or leaving the NATL domain. IBTrACS is also shown for reference, with "ET" being defined by a named TC having being tagged as "extratropical" in the storm-type variable at any point during its lifetime. As mentioned previously, it is important to remember that IBTrACS ET is not defined in the same manner as the four gridded data sets here.

Therefore, 40.4% and 48.8% of TCs undergo ET in the CAM-55 and CAM-28 data sets, respectively. In the CFSR (ERA-I) data, 50.0% (55.2%) of TCs undergo ET. In comparison, *Hart and Evans* [2001] found that 46% of Atlantic TCs between 1950 and 1996 transitioned to ETCs, according to NHC records and 2.5° ECMWF reanalysis data. *Studholme et al.* [2015] found that 67% of Atlantic storms transitioned to extratropical during

Table 1. Cumulative Climatology of Objectively Tracked TCs in CAM, CFSR, and ERA-I Over 1980–2002 (23 Years), Including Number of TCs, Number of ETs, and Total Percentage of Storms That Undergo ET[a]

Data Set	TCs	ETs	% Transition
CAM-55	178	72	40.4
CAM-28	248	121	48.8
CFSR	172	86	50.0
ERA-I	87	48	55.2
IBTrACS	246	113	45.9

[a]IBTrACS observations are also included for reference.

2008–2012 when applying a cluster analysis to high-resolution ECMWF operational forecast analyses with T255 (∼60 km) resolution. NATL ET fraction is 45.9% when using IBTrACS data between 1980 and 2002. Therefore, the results for all gridded data using the algorithm here fall in the range of published estimates, although the moderate amount of spread underscores uncertainty in quantifying ET, even in an ocean basin such as the North Atlantic, which has been subject to intensive research.

The seasonal cycles of TCs and corresponding ETs are shown in Figure 6. The total number of TCs in each month are shown by black bars, with the subset of those undergoing ET denoted by overlaid gray bars. IBTrACS observations are shown in Figure 6e.

In all data sets, the majority of the TCs occur between August and October (inclusive), considered to be the peak of the NATL TC season. All gridded results (Figures 6a–6d) correctly have TC activity peaking in September, in agreement with IBTrACS (Figure 6e). However, the second-most active month in both CAM simulations is October, unlike August in both reanalyses and IBTrACS, indicating a shift toward a slightly later TC
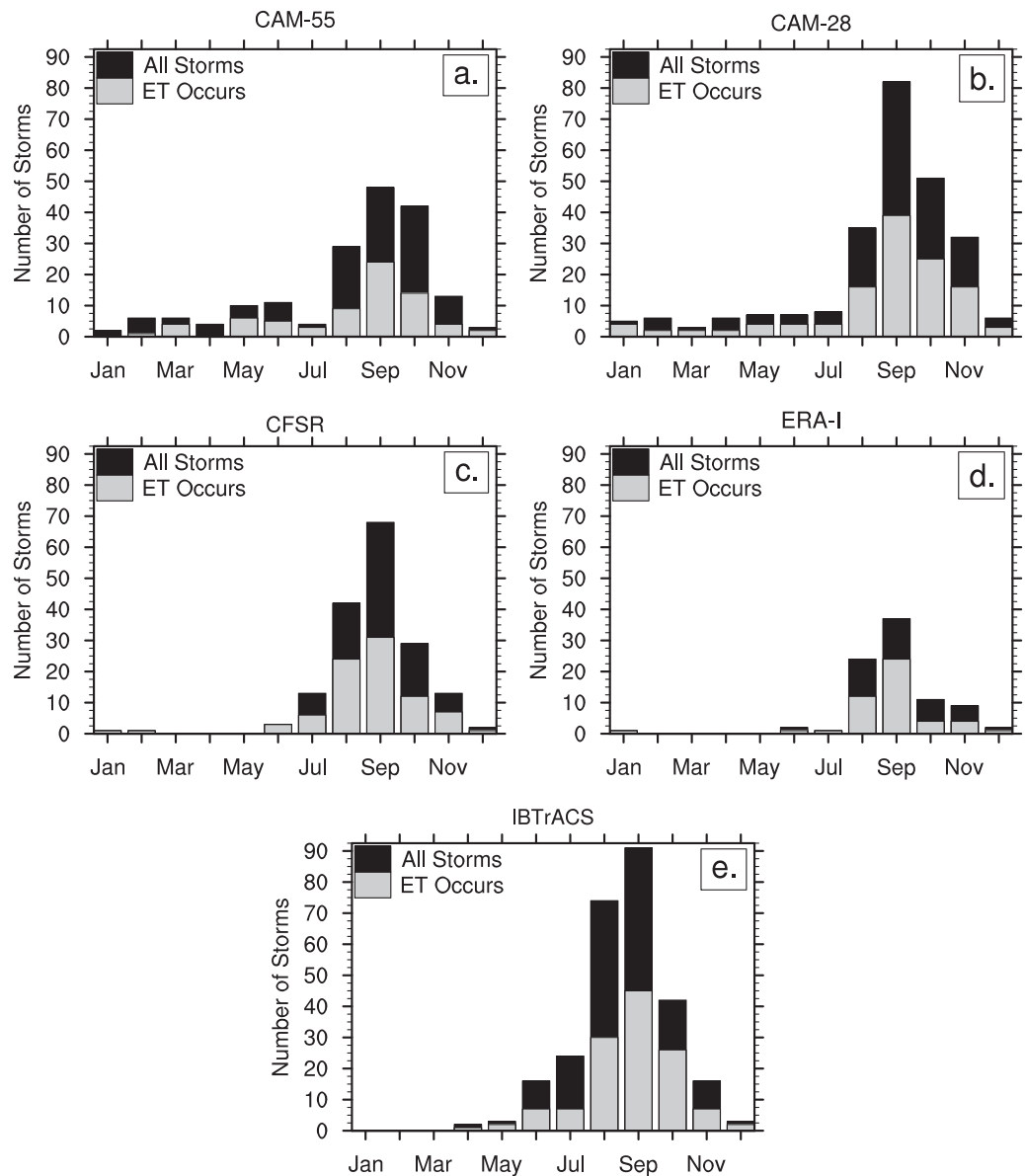

Figure 6. Monthly climatology showing total number of objectively tracked North Atlantic TCs (black) and number of TCs determined to undergo ET (gray) over the 1980–2002 period in (a) CAM-55, (b) CAM-28, (c) CFSR, and (d) ERA-I. The number of TCs as observed in the IBTrACS data set are shown in Figure 6e for comparison.

season peak (by storm count) in CAM. The ET cycle is fairly well matched between the data sets, with the peak number of ETs also occurring during September and the most active months for cumulative ETs also being August–November (inclusive).

Both CAM simulations produce a small, but nonnegligible number of TCs (and ETs) outside of the Atlantic TC season (January–May). This result was also noted in *Zarzycki and Jablonowski* [2014]. These results are robust for both CAM runs even though factors such as output horizontal resolution have been controlled for. A brief subjective analysis shows that many of these storms are relatively weak and they may be induced by large-scale biases in the climate state or other model deficiencies such as incorrect air-sea coupling [*Zarzycki et al.*, 2016; *Zarzycki*, 2016].

Figure 6 implies that the absolute number of ETs are strongly tied to the absolute number of TCs. Therefore, the ET seasonal cycle is better depicted by assessing the fraction of TCs each month that undergo ET. Previous work has indicated that fractional NATL ET may vary by approximately 20% between months during the height of the TC season [*Hart and Evans*, 2001; *Studholme et al.*, 2015]. The ET ratio by month during the NATL TC season is shown in Figure 7. Wildly different fractions are shown in June and July, although as seen in Figure 6, this is largely due to the fact that only a small number of TCs occur during this period (therefore, a handful of ET events can dramatically influence the climatological fraction, even over the multidecadal sample here). Both CAM-55 and ERA-I produce small local maxima (minima) in September (August), respectively. CFSR and ERA-I also show similar behavior following the peak of the NATL TC season, with a small local minimum in ET fraction occurring during October. CAM-28 produces the least variable ET fraction, with a shallow minimum in August and a slight increase each month thereafter until the end of the TC season. For August–November, the maximum-minimum spread between the data sets is no more than 25% in any given month.

Hart and Evans [2001] indicated that, over the 1979–1993 period, the maximum fraction of ET (relative to TCs) occurred during September and October. They demonstrated that this occurs due to the fact that the
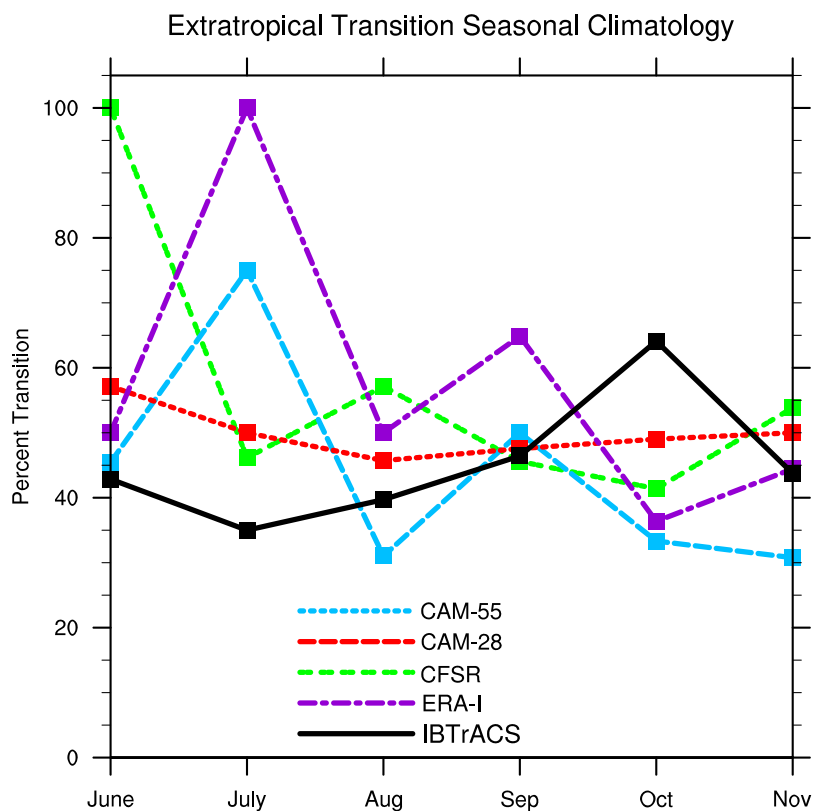

Figure 7. Percentage of TCs in CAM-55 (blue), CAM-28 (red), CFSR (green), ERA-I (purple), and IBTrACS (black) that undergo ET each month from June to November.

spatial distance between regions supporting TC development and extratropical development is smallest during this period. Here a slight local minimum in October occurs in both reanalyses as well as CAM-55, indicating that this minor discrepancy with *Hart and Evans* [2001] is not likely a function of large-scale climate biases (since CFSR and ERA-I are strongly constrained by observations and therefore should reproduce the correct dynamics supporting both tropical and extratropical development). It is worth pointing out that the some of the seasonal cycles of ET shown in Figure 7 are quite similar to those shown in *Studholme et al.* [2015, Figure 15a]. This, combined with the fact that the maximum in *Hart and Evans* [2001] is fairly shallow, would indicate that there is likely some uncertainty in projecting the seasonal fractionation of ET versus no-ET. A larger sample of TCs might help further constrain the seasonal evolution of NATL ET in both models and observations, although this is left to a future endeavor.

Storm trajectory analyses for CAM-SE, CFSR, and ERA-I (Figure 8) show the paths of all tracked storms in addition to the locations where ET begins (red, filled circle) and ends (blue, hollow square) for storms that
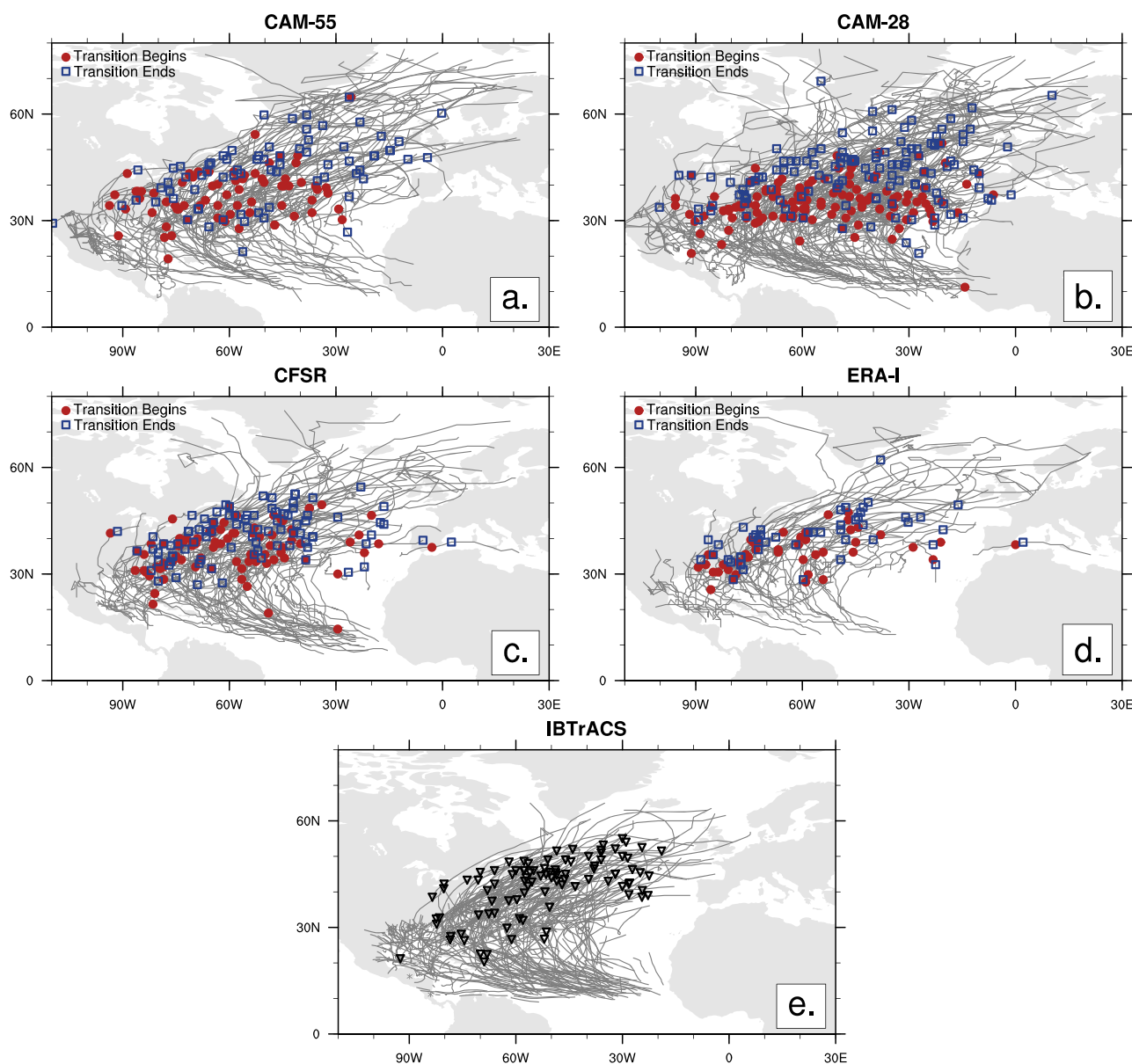

Figure 8. Objectively tracked storm trajectories from 1980 to 2002 for (a) CAM-55, (b) CAM-28, (c) CFSR, and (d) ERA-I. In Figures 8a–8d, gray lines indicate the full trajectory from TC genesis to ETC lysis, red circles indicate the beginning of ET, and blue squares indicate the completion of ET. IBTrACS trajectories are shown in Figure 8e with instantaneous ET being denoted by black triangles.

undergo ET. IBTrACS trajectories for all named TCs are shown in Figure 8e, with the first notation of extratropical structure during each TC's lifecycle denoted by a black triangle. Even though CAM-55, CFSR, and ERA-I have fewer storms than IBTrACS, storm trajectory lengths extend further north and east in Figures 8b–8d, demonstrating how the tracker continues following storms into the ETC phase. In both CAM simulations, some weaker systems are identified further east, near the coast of Africa (east of 25°W), than in the CFSR and ERA-I. Given that the CFSR resolution lies between the two CAM simulations and an identical TC tracking algorithm is used, this appears to represent a model bias where CAM spins up storms that trigger the tracking algorithm earlier in their lifecycle. However, the overall patterns between the top four plots look quite similar and are well matched to IBTrACS point observations. Many storms are initiated within the Atlantic Main Development Region (MDR) [*Goldenberg and Shapiro*, 1996] and generally track westward before typically recurving to the north and eventually the east. In a mean sense, recurvature is associated with the onset of ET transition, with ET terminating once the storm begins moving more eastward in the midlatitudes. One noticeable difference between CAM and the two reanalyses is that ET termination seems to occur further along in the general trajectory of TCs, with it occurring further to the north and east in both CAM simulations.

This spatial ET bias can be more conclusively highlighted in the median latitude and longitude of ET over the 23 year sampling period, shown in Figure 9. The latitude of ET onset (Figure 9a) is roughly the same between all four data sets, with medians ranging from roughly 35°N for CAM-28 to 38°N for CFSR. However, the latitude of ET termination is further north in both CAM simulations when compared to either CFSR or ERA-I, indicating a longer meridional distance to undergo ET. This can also be concluded (in the zonal direction) from corresponding plots for longitude (Figure 9b), where ET completion occurs further east for CAM. In fact, the median longitude of transition completion for CAM-28 is further east than the easternmost quartile of either CFSR or ERA-I.

Given that the spatial differences are larger at the end of ET rather than the onset, this implies that TCs in CAM take longer to undergo ET than the observationally forced CFSR, assuming there are no large biases in translation speed. The median (mean) start-to-finish duration of transition of all ET events in CFSR and ERA-I was 18 and 18 (34.7 and 40) h, compared to 36 (57.2) h for CAM-28 and 36 (50.9) h for CAM-55. *Evans and Hart* [2003] found a mean transition duration of 33.4 h in the NATL, using similar criteria for the start and end of transition, which agrees more closely with both observational reanalyses. Therefore, the tracking algorithm is doing a suitable job finding TCs and their subsequent ET in CFSR and ERA-I and that the increased duration length seen in CAM is not a function of the algorithm, but rather, appears to be a model behavior impacting the length of ET.
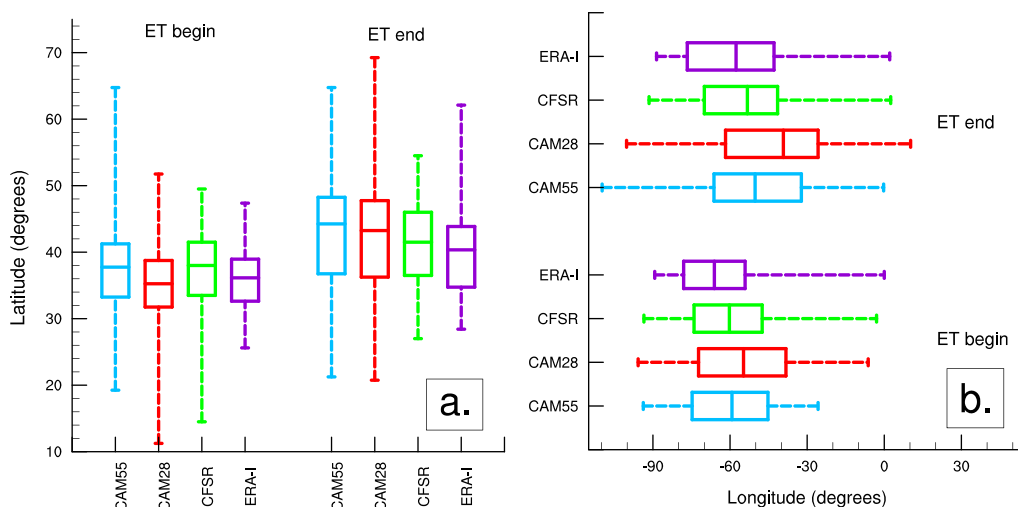

Figure 9. Boxplots showing aggregate statistics of both (a) latitude and (b) longitude of ET onset and completion in the North Atlantic. The bottom (left most) whisker denotes the minimum latitude (longitude) of ET. The top (right most) whisker denotes the maximum latitude (longitude) of ET. The bottom, middle, and top (left, middle, and right) lines that make up each box represent the 25th percentile, median, and 75th percentile latitude (longitude) of ET in each data set.

Table 2. ET Statistics for CAM-55, CAM-28, CFSR, and ERA-I Over the 1980–2002 Period[a]

	#	%	ET Dur. (h)	$SLP_{ET,st}$	$SLP_{ET,end}$	$SLP_{ETC,min}$
CAM-55						
All ET	72		36	987.7	993.2	988.3
Type I	50	69	42	979.5	990.6	985.2
Type II	21	29	18	1006.5	998.8	994.9
Type III	1	1	0	1003.9	1003.9	1003.7
CAM-28						
All ET	121		36	988.7	996.4	990.6
Type I	82	68	54	980.8	992.2	986.4
Type II	31	26	24	1005.4	1005.4	998.8
Type III	8	7	0	1003.9	1003.9	1002.2
CFSR						
All ET	86		18	998.8	999.5	993.6
Type I	49	57	24	995.4	997.3	991.7
Type II	29	34	12	1004.4	1003.4	996.7
Type III	8	9	0	998.9	998.9	994.1
ERA-I						
All ET	48		18	998.5	998.9	991.6
Type I	25	52	24	992.5	992.8	988.3
Type II	22	46	12	1005.1	1005.6	994.8
Type III	1	2	0	1002.7	1002.7	1002.7

[a]Included are statistics for all ET events as well as ET events broken down by pathway (defined in text). Shown are the total number of cases (#), percentage of ET per data set for each type (%), median duration of ET (ET Dur.), and mean storm SLP at ET onset ($SLP_{ET,st}$) and ET conclusion ($SLP_{ET,end}$) as well as mean minimum SLP achieved post-ET ($SLP_{ETC,min}$).

Using objective phase space analysis to quantify ET also provides for dynamical insight into how ET occurs. The ET behavior for each data set can be further subdivided by path to ET, as in *Studholme et al.* [2015]. This is due to the fact that the objective technique outlined above allows a TC to transition from symmetric warm core to asymmetric cold core via three separate pathways. The vast majority of NATL TCs that undergo ET do so by going through the asymmetric warm-core sector (i.e., in Figure 2a, the B threshold is satisfied first, storm follows a counter-clockwise path through CPS, denoted as Type I here) [*Hart*, 2003]. However, with this algorithm, TCs may also pass through the symmetric cold-core structure first (in Figure 2a, the $-V_T^L$ criteria is first satisfied, storm follows clockwise path through CPS, Type II) or pass directly to asymmetric cold core (both ET criteria are satisfied at the same 6 hourly time step, Type III). Table 2 shows the fraction that follow each of these three pathways as well as their median duration of ET, mean SLP at ET onset and completion, and the mean minimum SLP achieved following ET (i.e., maximum intensity the storm reaches after becoming a full-fledged ETC). Type III storms will always have a duration of 0 h because they satisfy both ET criteria at the same time step.

In all four data sets, the majority of storms become asymmetric first before becoming cold core (Type I). This fraction ranges from 52% in the ERA-I to 69% in CAM-55. *Studholme et al.* [2015] found the majority of global ETs actually occurred by developing a cold core before losing symmetry (Type II). However, *Hart* [2003] has noted that the majority of ETs in the NATL basin follow the same Type I pathway as the most popular route in this study, signifying that the fractional breakdown of ET pathway varies significantly from ocean basin to ocean basin. This is also confirmed by *Wood and Ritchie* [2014] who found that the Type I pathway was preferred by TCs in both the NATL and northwestern Pacific basins, with Type II transitions occurring more frequently in the northeastern Pacific.

Storms following the more common Type I pathway tend to have longer ET durations than either Type II or III. This demonstrates that the "long" bias in ET duration in CAM is primarily tied to Type I storms, with the median duration for this case being approximately twice as long for both CAM simulations compared to CFSR and ERA-I. Median durations for Type II transitions, on the other hand, are within 12 h of each other for all products. Storms following the Type I path are the strongest at both ET onset and completion across all data sets, implying that this is the preferred pathway for more intense TCs. Aside from the mean SLP at ET end in CAM-55, all SLP during ET for Type II transitions are weaker than 1000 hPa for all four data sets. This intensity signal appears to persist even as storms become fully fledged ETCs, with the mean minimum SLP a storm reaches following ET termination ($SLP_{ETC,min}$) being universally strongest for Type I storms. Of note, lesser grid resolution sensitivity exists in intensity (e.g., between CAM-55 and CAM-28) after a storm begins undergoing ET when compared to storms in the TC phase (Figure 5). This is to be expected as ETCs are larger systems and, when applying a scale analysis, are predicted to be well resolved at all resolutions in this study [*Holton*, 2004].

As noted in Figure 6, both CAM simulations produce TCs and ET in months outside of the typical NATL TC season. It is possible that these storms are forming further away from the tropics and spending more time in phases between ET start and ET completion, biasing the results. To assess this, boxplots were also computed by only considering TCs between the months of June and November (inclusive) (Figure 10). It is
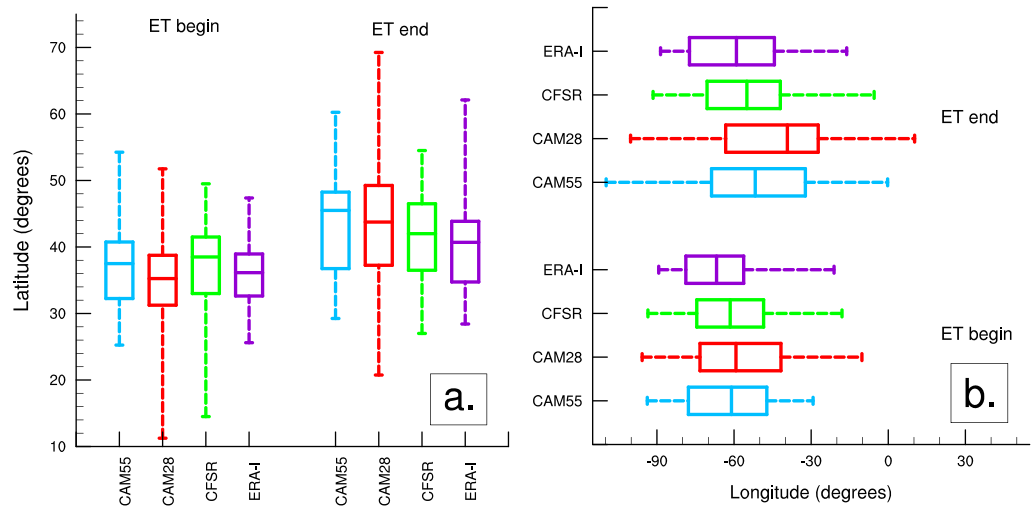
Figure 10. Same as Figure 9 except only considering ET that occurs during the North Atlantic tropical season (June–November).

obvious that the same general behaviors are evident even when only examining storms occurring during the defined NATL TC season (in a mean sense, CAM producing ET that ends further north and east). This appears to indicate that the spatiotemporal differences seen in ET between CAM and observational reanalyses indeed arise due to fundamental differences in the representation of TCs and ET themselves rather than as a secondary effect of sampling more nontraditional TCs out-of-season.

4.2. Cyclone Phase Space
Figure 11 shows the cyclone phase space probability density function (PDF) of each 6 h point along each TC/ETC trajectory during the entire lifetime of all storms in all four data sets as 2-D histograms. All plots are
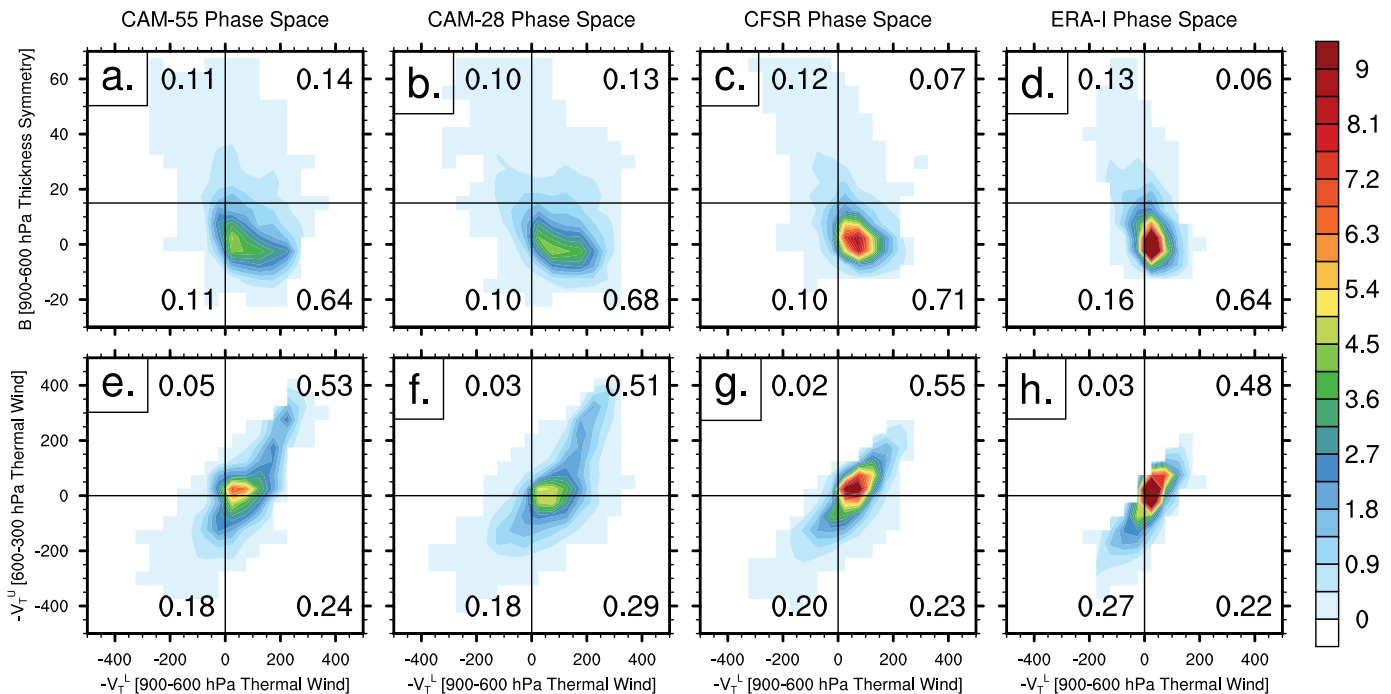

Figure 11. Two-dimensional histogram of phase space distribution for all tracked cyclones in (a, e) CAM-55, (b, f) CAM-28, (c, g) CFSR, and (d, h) ERA-I. B and $-V_T^L$ are shown on the top, $-V_T^U$ and $-V_T^L$ on the bottom. Color contouring denotes density of points when 2-D space is broken into 20-by-20 grid. Fraction of points that lie within each quadrant are overlaid as text annotations and may not sum to exactly 1.0 due to rounding.

normalized to the total number of storms in each data set. The fraction of data points that lie in each quadrant are overlaid as text annotations.

Tracked points are predominately distributed within the symmetric warm-core regime (SWC, lower right) in Figures 11a–11d (compare to Figure 2a). The primary reason for this is the contribution of the tropical phase of all trajectories. Additionally, a large fraction of the storms, 51% (60%) in the CAM-28 (CAM-55) simulation and 50% (45%) in CFSR (ERA-I) data never undergo ET, meaning they never (or only briefly) leave the SWC quadrant. There is larger spread within this quadrant for both CAM simulations when compared to CFSR or ERA-I, although all four data sets agree with approximately two-thirds of cyclone points being SWC. This implies that a larger SWC variance exists in this region as opposed to a fundamental shift in the absolute number. While the fraction of points is also similar in the symmetric cold core sector (SCC, lower left) for all four data sets, larger differences appear when storms are asymmetric. In particular, CFSR and ERA-I have lower fractions of data points that are asymmetric warm core (AWC, top right) and higher fraction in the asymmetric cold core (ACC, top left) when compared to CAM. This is intuitive and agrees with two results from the previous section. One, CAM has a larger fraction of storms that undergo Type I transitions (via the AWC sector). Second, storms in CAM tend to take longer to undergo ET (particularly for Type I transitions). Both of these facts result in cyclones in CAM that spend a larger fraction of their lifetimes in the top right (AWC) quadrant.

Figures 11e–11h, bottom, show a predominately linear relationship between the thermal structure in the upper and lower troposphere (compare to Figure 2b). Both CAM simulations produce very deep warm-core cyclones, where $-V_L^T$ and $-V_U^T$ are greater than 200, values that rarely occur in CFSR or ERA-I (top right quadrants). CAM therefore produces a larger proportion of stronger, deeper warm-core TCs, in agreement with the intensity statistics presented earlier. Increasing resolution (from CAM-55 to CAM-28) increases the variance (more diffuse PDF), which is particularly evident in the upper level warm-core spread, demonstrating that a large component of the resolution intensity signature in CAM (Figure 5) can be more overtly seen in the overall depth of the TC's warm core (as opposed to, for example, cyclone symmetry). While differences between CAM and the reanalyses are not as obvious in each quadrant's cumulative frequency as Figures 11a–11d, an ET duration signal can still be seen in Figures 11e–11h. Cyclones in CFSR and ERA-I spend more time in the deep cold-core phase, indicating less time spent in transitionary quadrants (top left, lower right) and a higher fraction of storm lifetime spent as a well-defined ETC (lower left).

Both the top and bottom sets of plots look relatively similar in aggregate and are well matched to observational CPS density plots [*Hart*, 2003; *Kitabatake*, 2011; *Wood and Ritchie*, 2014; *Studholme et al.*, 2015], offering additional confirmation that, even though the objective technique here cannot necessarily reproduce the precise number of TCs (and therefore ET) seen in the observation record, that the mean behavior of TCs and their ET can be faithfully reproduced in high-resolution climate models and can be detected using automated means.

5. Discussion and Conclusions

This paper demonstrates an objective technique for detecting the extratropical transition of tropical cyclones in high-resolution gridded climate data. In particular, objective parameters defined by *Hart* [2003] are calculated during storm lifetime to construct a cyclone phase space that defines both the vertical thermal structure and asymmetry of the cyclone. This phase space is used to indicate when a cyclone is in the tropical phase, when it is undergoing transition, and when it is purely an extratropical cyclone.

TCs have been objectively tracked in high-resolution climate model data by many groups [*Walsh et al.*, 2015], but to our knowledge, there have been no studies which attempt to extend their evaluation to a longer lifetime by rigorously quantifying cyclone behavior following the onset of extratropical transition (when the storms are no longer in the tropical phase). This algorithm requires multiple gridded fields that are continuous in space and time, which makes comparison of model results to historical point observations (e.g., IBTrACS) difficult due to the fact that the same observational data set is impossible to reproduce for climate model output. This incompatibility between point storm observations and gridded data adds uncertainty in determining how faithfully models represent dynamical processes associated with TCs. Reanalysis data (such as CFSR and ERA-I) can be thought of as highly constrained global climate models, thereby offering proxies for assessing model performance relative to the historical record by allowing for a more consistent

comparison when analyzing climate model data. While a manual tracking analysis could be applied to reanalysis products to find all observed TCs in the historical record, this would not provide a sufficient comparison with climate model data given the lack of a priori points to use in such an application. Therefore, we apply an objective algorithm to CFSR and ERA-I data as a basis for comparison with CAM data, ensuring that model data are analyzed at the same horizontal resolution (thereby controlling for output grid). That the CAM grid spacing straddles the CFSR resolution also allows for rudimentary segregation of resolution and non-resolution differences in simulated storm climatology.

In this study, focus is centered on the North Atlantic basin via the application of variable-resolution CAM and domain-restricted tracking. When compared to previously published observational studies investigating NATL ET, objectively tracked storms are realistic, persisting as deep, symmetric, warm-core features at low latitudes before undergoing transition to asymmetric cold-core features after recurvature into the midlatitudes. Generally, all products produce fewer TCs when compared to IBTrACS and this low bias is more noticeably manifested in storm intensity. This agrees with previous work that shows TCs in high-resolution climate models are better represented than their low-resolution counterparts, but remain underresolved at these grid spacings. However, the importance of model configuration is also evident, with CAM-55 producing a stronger intensity profile than CFSR, even though TCs in CFSR are resolved at a higher nominal grid spacing. This discrepancy may result from differences in the dynamical core [e.g., *Zhao et al.*, 2012; *Reed et al.*, 2015], subgrid physical parameterizations [e.g., *Reed and Jablonowski*, 2011; *Lim et al.*, 2014], or both.

The use here of an algorithm that tracks TC ET and subsequent ETCs demonstrates that differences between CFSR or ERA-I and CAM exist beyond the commonly tracked tropical phase. Both CFSR and ERA-I ET statistics are well matched in a mean sense to previous observational studies [*Hart*, 2003; *Evans and Hart*, 2003], establishing that the tracking technique here adequately identifies average TC/ET behavior in observational reanalyses. Further, CFSR and ERA-I are relatively similar to one another, despite differences in how TCs are specifically assimilated into the reanalyses, lending confidence that statistics produced by the two as "observational proxies" are robust.

The mean latitude of ET completion is further north in both CAM simulations. Combined with longer ET durations, this demonstrates that storms take noticeably longer to undergo transition in the North Atlantic mid-latitudes in CAM. This bias is common in both CAM-55 and CAM-28 simulations and stems from differences in the behavior of Type I transitions (i.e., TCs in CAM take longer to lose their warm core after becoming asymmetric when compared to CFSR). Therefore, CAM appears to have a different dynamical representation of ET, which may arise from differences in the mean midlatitude flow (and subsequent TC interaction with this flow) or the parameterized physical processes important to ET (e.g., convection, microphysics, and surface fluxes). On average, TCs are slightly weaker when entering ET in the reanalyses, indicating that they may require less time in either the SCC or AWC sectors of the CPS before becoming ACC. However, there is not a significant resolution signal in the resulting ETCs post-ET, likely due to the fact that all grid spacings can well resolve the broader dynamical fields associated with ETCs.

CAM produces more out-of-season (December–May) TCs and ET than either CFSR, ERA-I, or IBTrACS. However, differences in ET duration and transition location for storms in and out of the North Atlantic TC season were not statistically or noticeably different. Because CAM was integrated at multiple resolutions and an identical tracker was used strongly implies that this behavior is a bias in CAM rather than an issue with sampling storms. This highlights that simulated TC/ET annual cycles should be considered when using cumulative storm counts for comparisons between modeled cyclones and observations. The exact reasons why a nonnegligible fraction of TC/ET events occur out-of-season and why storms that undergo ET in CAM behave differently compared to CFSR and ERA-I are key targets for future research. The tracking method outlined here offers new avenues for model improvements as researchers better understand the simulation of climate extremes at higher resolutions. Multimodel intercomparisons applying this technique may prove particularly insightful into understanding uncertainty in simulated TC climatology.

While these data primarily focus on tracking single-value properties (at each time step) associated with storm intensity following ET, the addition of objective phase space tracking to TC lifetime will allow for additional analysis of the dynamical behavior of storms undergoing ET. For example, one common response of TCs undergoing ET is for their wind field to become much larger in response to increased baroclinicity

[*Jones et al.*, 2003; *Evans and Hart*, 2008]. Future work may not only investigate the extent of TC wind fields in climate data [*Reed and Chavas*, 2015], but also the corresponding wind and precipitation field changes associated with ET and how these properties might be impacted by a changing climate.

References

Anwender, D., P. A. Harr, and S. C. Jones (2008), Predictability associated with the downstream impacts of the extratropical transition of tropical cyclones: Case studies, *Mon. Weather Rev.*, *136*(9), 3226–3247, doi:10.1175/2008MWR2249.1.

Bacmeister, J. T., M. F. Wehner, R. B. Neale, A. Gettelman, C. Hannay, P. H. Lauritzen, J. M. Caron, and J. E. Truesdale (2014), Exploratory high-resolution climate simulations using the Community Atmosphere Model (CAM), *J. Clim.*, *27*(9), 3073–3099, doi:10.1175/JCLI-D-13-00387.1.

Bengtsson, L., K. I. Hodges, M. Esch, N. Keenlyside, L. Kornblueh, J.-J. Luo, and T. Yamagata (2007), How may tropical cyclones change in a warmer climate?, *Tellus, Ser. A*, *59*(4), 539–561, doi:10.1111/j.1600-0870.2007.00251.x.

Brown, D. P. (2013), Tropical cyclone report: Hurricane Nadine, *Tech. Rep.* #AL142012, Natl. Hurricane Cent., 19, Miami, Fla.

Dee, D. P., et al. (2011), The ERA-Interim reanalysis: Configuration and performance of the data assimilation system, *Q. J. R. Meteorol. Soc.*, *137*(656), 553–597, doi:10.1002/qj.828.

Dennis, J. M., J. Edwards, K. J. Evans, O. Guba, P. H. Lauritzen, A. A. Mirin, A. St-Cyr, M. A. Taylor, and P. H. Worley (2012), CAM-SE: A scalable spectral element dynamical core for the Community Atmosphere Model, *Int. J. High Performance Comput. Appl.*, *26*(1), 74–89, doi:10.1177/1094342011428142.

DiMego, G. J., and L. F. Bosart (1982), The transformation of Tropical Storm Agnes into an extratropical cyclone. Part I: The observed fields and vertical motion computations, *Mon. Weather Rev.*, *110*(5), 385–411, doi:10.1175/1520-0493(1982)110<0385:TTOTSA>2.0.CO;2.

Evans, C., and R. E. Hart (2008), Analysis of the wind field evolution associated with the Extratropical Transition of Bonnie (1998), *Mon. Weather Rev.*, *136*(6), 2047–2065, doi:10.1175/2007MWR2051.1.

Evans, J. L., and R. E. Hart (2003), Objective indicators of the life cycle evolution of extratropical transition for Atlantic tropical cyclones, *Mon. Weather Rev.*, *131*(5), 909–925, doi:10.1175/1520-0493(2003)131<0909:OIOTLC>2.0.CO;2.

Foley, G., and B. Hanstrum (1994), The capture of tropical cyclones by cold fronts off the west coast of Australia, *Weather Forecast.*, *9*(4), 577–592, doi:10.1175/1520-0434(1994)009<0577:TCOTCB>2.0.CO;2.

Gates, W. L. (1992), AMIP: The atmospheric model intercomparison project, *Bull. Am. Meteorol. Soc.*, *73*(12), 1962–1970, doi:10.1175/1520-0477(1992)073<1962:ATAMIP>2.0.CO;2.

Gleckler, P. J. (Ed.) (2004), *The Second Phase of the Atmospheric Model Intercomparison Project (AMIP2): Toward Innovative Model Diagnostics*, 253 pp., Météo-France, Toulouse, France.

Goldenberg, S. B., and L. J. Shapiro (1996), Physical mechanisms for the association of El Niño and West African rainfall with Atlantic major hurricane activity, *J. Clim.*, *9*(6), 1169–1187, doi:10.1175/1520-0442(1996)009<1169:PMFTAO>2.0.CO;2.

Harr, P. A., and R. L. Elsberry (2000), Extratropical transition of tropical cyclones over the western North Pacific. Part I: Evolution of structural characteristics during the transition process, *Mon. Weather Rev.*, *128*(8), 2613–2633, doi:10.1175/1520-0493(2000)128<2613:ETOT-CO>2.0.CO;2.

Harr, P. A., R. L. Elsberry, and T. F. Hogan (2000), Extratropical transition of tropical cyclones over the western North Pacific. Part II: The impact of midlatitude circulation characteristics, *Mon. Weather Rev.*, *128*(8), 2634–2653, doi:10.1175/1520-0493(2000)128<2634:ETOT-CO>2.0.CO;2.

Hart, R. E. (2003), A cyclone phase space derived from thermal wind and thermal asymmetry, *Mon. Weather Rev.*, *131*(4), 585–616, doi:10.1175/1520-0493(2003)131<0585:ACPSDF>2.0.CO;2.

Hart, R. E., and J. L. Evans (2001), A climatology of the extratropical transition of Atlantic tropical cyclones, *J. Clim.*, *14*(4), 546–564, doi:10.1175/1520-0442(2001)014<0546:ACOTET>2.0.CO;2.

Hart, R. E., J. L. Evans, and C. Evans (2006), Synoptic composites of the extratropical transition life cycle of North Atlantic tropical cyclones: Factors determining posttransition evolution, *Mon. Weather Rev.*, *134*(2), 553–578, doi:10.1175/MWR3082.1.

Holton, J. R. (2004), *An Introduction to Dynamic Meteorology*, 535 pp., Elsevier, New York.

Hurrell, J. W., J. J. Hack, D. Shea, J. M. Caron, and J. Rosinski (2008), A new sea surface temperature and sea ice boundary dataset for the Community Atmosphere Model, *J. Clim.*, *21*(19), 5145–5153, doi:10.1175/2008JCLI2292.1.

Jarvinen, B., C. Neumann, and M. Davis (1984), A tropical cyclone data tape for the North Atlantic Basin, 1886–1983: Contents, limitations, and uses, *Tech. Memo. NWS NHC 22*, Natl. Oceanic Atmos. Admin., Miama, Fla.

Jones, S. C., et al. (2003), The extratropical transition of tropical cyclones: Forecast challenges, current understanding, and future directions, *Weather Forecast.*, *18*(6), 1052–1092, doi:10.1175/1520-0434(2003)018<1052:TETOTC>2.0.CO;2.

Kitabatake, N. (2011), Climatology of extratropical transition of tropical cyclones in the western North Pacific defined by using cyclone phase space, *J. Meteorol. Soc. Jpn.*, *89*(4), 309–325, doi:10.2151/jmsj.2011-402.

Klein, P. M., P. A. Harr, and R. L. Elsberry (2000), Extratropical transition of western North Pacific tropical cyclones: An overview and conceptual model of the transformation stage, *Weather Forecast.*, *15*(4), 373–395, doi:10.1175/1520-0434(2000)015<0373:ETOWNP>2.0.CO;2.

Knapp, K. R., M. C. Kruk, D. H. Levinson, H. J. Diamond, and C. J. Neumann (2010), The international best track archive for climate steward-ship (IBTrACS), *Bull. Am. Meteorol. Soc.*, *91*(3), 363–376, doi:10.1175/2009BAMS2755.1.

Krishnamurti, T. N., D. Oosterhof, and N. Dignon (1989), Hurricane prediction with a high resolution global model, *Mon. Weather Rev.*, *117*(3), 631–669, doi:10.1175/1520-0493(1989)117<0631:HPWAHR>2.0.CO;2.

Landsea, C. W., and J. L. Franklin (2013), Atlantic hurricane database uncertainty and presentation of a new database format, *Mon. Weather Rev.*, *141*(10), 3576–3592, doi:10.1175/MWR-D-12-00254.1.

Lim, Y.-K., S. D. Schubert, O. Reale, M.-I. Lee, A. M. Molod, and M. J. Suarez (2014), Sensitivity of tropical cyclones to parameterized convec-tion in the NASA GEOS-5 model, *J. Clim.*, *28*(2), 551–573, doi:10.1175/JCLI-D-14-00104.1.

McAdie, C., C. Landsea, C. Neumann, J. David, E. Blake, and G. Hammer (2009), *Tropical Cyclones of the North Atlantic Ocean, 1851-2006, Hist. Climatol. Ser.*, vol. *6-2*, 238 pp., Natl. Clim. Data Cent.

Murakami, H. (2014), Tropical cyclones in reanalysis data sets, *Geophys. Res. Lett.*, *41* 2133–2141, doi:10.1002/2014GL059519.

Neale, R. B., et al. (2010), Description of the NCAR Community Atmosphere Model (CAM 5.0), *NCAR Tech. Note NCAR/TN-486+STR*, 268 pp., Natl. Cent. for Atmos. Res., Boulder, Colo.

Oleson, K. W., et al. (2010), Technical description of version 4.0 of the Community Land Model (CLM), *NCAR Tech. Note NCAR/TN-478+STR*, 257 pp., Natl. Cent. for Atmos. Res., Boulder, Colo.

Reed, K. A., and D. R. Chavas (2015), Uniformly rotating global radiative-convective equilibrium in the community atmosphere model, version 5, *J. Adv. Model. Earth Syst.*, *7*, 1938–1955, doi:10.1002/2015MS000519.

Reed, K. A., and C. Jablonowski (2011), Impact of physical parameterizations on idealized tropical cyclones in the Community Atmosphere Model, *Geophys. Res. Lett.*, *38*, L04805, doi:10.1029/2010GL046297.

Reed, K. A., J. T. Bacmeister, N. A. Rosenbloom, M. F. Wehner, S. C. Bates, P. H. Lauritzen, J. E. Truesdale, and C. Hannay (2015), Impact of the dynamical core on the direct simulation of tropical cyclones in a high-resolution global model, *Geophys. Res. Lett.*, *42*, 3603–3608, doi: 10.1002/2015GL063974.

Ritchie, E. A., and R. L. Elsberry (2001), Simulations of the transformation stage of the extratropical transition of tropical cyclones, *Mon. Weather Rev.*, *129*(6), 1462–1480, doi:10.1175/1520-0493(2001)129<1462:SOTTSO>2.0.CO;2.

Ritchie, E. A., and R. L. Elsberry (2003), Simulations of the extratropical transition of tropical cyclones: Contributions by the midlatitude upper-level trough to reintensification, *Mon. Weather Rev.*, *131*(9), 2112–2128, doi:10.1175/1520-0493(2003)131<2112:SOTETO>2.0.CO;2.

Ritchie, E. A., and R. L. Elsberry (2007), Simulations of the extratropical transition of tropical cyclones: Phasing between the upper-level trough and tropical cyclones, *Mon. Weather Rev.*, *135*(3), 862–876, doi:10.1175/MWR3303.1.

Saha, S., et al. (2010), The NCEP climate forecast system reanalysis, *Bull. Am. Meteorol. Soc.*, *91*, 1015–1057.

Schenkel, B. A., and R. E. Hart (2012), An examination of tropical cyclone position, intensity, and intensity life cycle within atmospheric reanalysis datasets, *J. Clim.*, *25*(10), 3453–3475, doi:10.1175/2011JCLI4208.1.

Simpson, R. H. (1974), The hurricane disaster—Potential scale, *Weatherwise*, *27*(4), 169–186, doi:10.1080/00431672.1974.9931702.

Sinclair, M. R. (1993), Synoptic-scale diagnosis of the extratropical transition of a southwest Pacific tropical cyclone, *Mon. Weather Rev.*, *121*(4), 941–960, doi:10.1175/1520-0493(1993)121<0941:SSDOTE>2.0.CO;2.

Sinclair, M. R. (2002), Extratropical transition of southwest Pacific tropical cyclones. Part I: Climatology and mean structure changes, *Mon. Weather Rev.*, *130*(3), 590–609, doi:10.1175/1520-0493(2002)130<0590:ETOSPT>2.0.CO;2.

Song, J., J. Han, and Y. Wang (2011), Cyclone phase space characteristics of the extratropical transitioning tropical cyclones over the western North Pacific, *Acta Meteorol. Sin.*, *25*(1), 78–90, doi:10.1007/s13351-011-0006-y.

Strachan, J., P. L. Vidale, K. Hodges, M. Roberts, and M.-E. Demory (2013), Investigating global tropical cyclone activity with a hierarchy of AGCMs: The role of model resolution, *J. Clim.*, *26*(1), 133–152, doi:10.1175/JCLI-D-12-00012.1.

Studholme, J., K. I. Hodges, and C. M. Brierley (2015), Objective determination of the extratropical transition of tropical cyclones in the Northern Hemisphere, *Tellus, Ser. A*, *67*, doi:10.3402/tellusa.v67.24474.

Taylor, M., J. Tribbia, and M. Iskandarani (1997), The spectral element method for the shallow water equations on the sphere, *J. Comput. Phys.*, *130*(1), 92–108, doi:10.1006/jcph.1996.5554.

Taylor, M. A., and A. Fournier (2010), A compatible and conservative spectral element method on unstructured grids, *J. Comput. Phys.*, *229*(17), 5879–5895, doi:10.1016/j.jcp.2010.04.008.

Ullrich, P. A., and M. A. Taylor (2015), Arbitrary-order conservative and consistent remapping and a theory of linear maps: Part I, *Mon. Weather Rev.*, *143*(6), 2419–2440, doi:10.1175/MWR-D-14-00343.1.

Ullrich, P. A., and C. M. Zarzycki (2016), Tempestextremes: A framework for scale-insensitive pointwise feature tracking on unstructured grids, *Geosci. Model Dev. Discuss.*, doi:10.5194/gmd-2016-217, in press.

Ullrich, P. A., D. Devendran, and H. Johansen (2016), Arbitrary-order conservative and consistent remapping and a theory of linear maps: Part II, *Mon. Weather Rev.*, *144*(4), 1529–1549, doi:10.1175/MWR-D-15-0301.1.

Walsh, K. J. E., M. Fiorino, C. W. Landsea, and K. L. McInnes (2007), Objectively determined resolution-dependent threshold criteria for the detection of tropical cyclones in climate models and reanalyses, *J. Clim.*, *20*(10), 2307–2314, doi:10.1175/JCLI4074.1.

Walsh, K. J. E., et al. (2015), Hurricanes and climate: The U.S. CLIVAR working group on hurricanes, *Bull. Am. Meteorol. Soc.*, *96*(6), 997–1017, doi:10.1175/BAMS-D-13-00242.1.

Wehner, M. F., et al. (2014), The effect of horizontal resolution on simulation quality in the Community Atmospheric Model, CAM5.1, *J. Adv. Model. Earth Syst.*, *6*, 980–997, doi:10.1002/2013MS000276.

Wood, K. M., and E. A. Ritchie (2014), A 40-year climatology of extratropical transition in the eastern North Pacific, *J. Clim.*, *27*(15), 5999–6015, doi:10.1175/JCLI-D-13-00645.1.

Zarzycki, C. M. (2016), Tropical cyclone climatology biases associated with prescribed sea surface temperatures in high-resolution global atmospheric experiments, *J. Clim.*, *29*, 8589–8610, doi:10.1175/JCLI-D-16-0273.1.

Zarzycki, C. M., and C. Jablonowski (2014), A multidecadal simulation of Atlantic tropical cyclones using a variable-resolution global atmospheric general circulation model, *J. Adv. Model. Earth Syst.*, *6*, 805–828, doi:10.1002/2014MS000352.

Zarzycki, C. M., C. Jablonowski, and M. A. Taylor (2014a), Using variable-resolution meshes to model tropical cyclones in the Community Atmosphere Model, *Mon. Weather Rev.*, *142*(3), 1221–1239, doi:10.1175/MWR-D-13-00179.1.

Zarzycki, C. M., M. N. Levy, C. Jablonowski, J. R. Overfelt, M. A. Taylor, and P. A. Ullrich (2014b), Aquaplanet experiments using CAM's variable-resolution dynamical core, *J. Clim.*, *27*, 5481–5503, doi:10.1175/JCLI-D-14-00004.1.

Zarzycki, C. M., C. Jablonowski, D. R. Thatcher, and M. A. Taylor (2015), Effects of localized grid refinement on the general circulation and climatology in the Community Atmosphere Model, *J. Clim.*, *28*(7), 2777–2803, doi:10.1175/JCLI-D-14-00599.1.

Zarzycki, C. M., K. A. Reed, J. T. Bacmeister, A. P. Craig, S. C. Bates, and N. A. Rosenbloom (2016), Impact of surface coupling grids on tropical cyclone extremes in high-resolution atmospheric simulations, *Geosci. Model Dev.*, *9*(2), 779–788, doi:10.5194/gmd-9-779-2016.

Zhao, M., I. M. Held, S.-J. Lin, and G. A. Vecchi (2009), Simulations of global hurricane climatology, interannual variability, and response to global warming using a 50-km resolution GCM, *J. Clim.*, *22*(24), 6653–6678, doi:10.1175/2009JCLI3049.1.

Zhao, M., I. M. Held, and S.-J. Lin (2012), Some counterintuitive dependencies of tropical cyclone frequency on parameters in a GCM, *J. Atmos. Sci.*, *69*(7), 2272–2283, doi:10.1175/JAS-D-11-0238.1.